J. Fluid Mech. (2000), *vol.* 415, *pp.* 65–87. Printed in the United Kingdom

© 2000 Cambridge University Press

Numerical study of internal wave–wave interactions in a stratified fluid

By A. JAVAM[1], J. IMBERGER[2] AND S. W. ARMFIELD[1]

[1] Department of Mechanical Engineering, University of Sydney, Sydney, 2006, Australia

[2] Department of Environmental Engineering, Centre for Water Research, University of Western Australia

(Received 6 June 1996 and in revised form 25 February 2000)

A finite volume method is used to study the generation, propagation and interaction of internal waves in a linearly stratified fluid. The internal waves were generated using single and multiple momentum sources. The full unsteady equations of motion were solved using a SIMPLE scheme on a non-staggered grid. An open boundary, based on the Sommerfield radiation condition, allowed waves to propagate through the computational boundaries with minimum reflection and distortion. For the case of a single momentum source, the effects of viscosity and nonlinearity on the generation and propagation of internal waves were investigated.

Internal wave–wave interactions between two wave rays were studied using two momentum sources. The rays generated travelled out from the sources and intersected in interaction regions where nonlinear interactions caused the waves to break. When two rays had identical properties but opposite horizontal phase velocities (symmetric interaction), the interactions were not described by a triad interaction mechanism. Instead, energy was transferred to smaller wavelengths and, a few periods later, to standing evanescent modes in multiples of the primary frequency (greater than the ambient buoyancy frequencies) in the interaction region. The accumulation of the energy caused by these trapped modes within the interaction region resulted in the overturning of the density field. When the two rays had different properties (apart from the multiples of the forcing frequencies) the divisions of the forcing frequencies as well as the combination of the different frequencies were observed within the interaction region.

The model was validated by comparing the results with those from experimental studies. Further, the energy balance was conserved and the dissipation of energy was shown to be related to the degree of nonlinear interaction.

1. Introduction

Overturning of internal waves and the resulting turbulence play an important role in the microscale dynamics of the atmosphere and the oceans (Gregg 1989; Fritts 1989). In the atmosphere, the generation of turbulence by the overturning of internal waves is a primary cause of clear air turbulence and a major source of internal mixing (Pao & Goldberg 1969). In the oceans and lakes, a range of instabilities lead to subsurface mixing including shear instabilities, convective instabilities, wave-shear instabilities, critical layer absorption, and wave–wave instabilities (Thorpe 1987*a*; Imberger & Ivey 1991; Imberger & Patterson 1990). The common feature of these sources of instabilities is an exchange between mean or wave kinetic energy and

https://doi.org/10.1017/S0022112000008594 Published online by Cambridge University Press

potential energy, after which time smaller-scale instabilities induce mixing causing an adjustment of the potential energy of the water column (Imberger & Ivey 1991).

Numerous experimental investigations of internal wave generation by bodies of finite dimensions with various shapes and motions have been reported. Monochromatic oscillations of a cylinder (Mowbray & Rarity 1967) and a sphere (McLaren, Pierce & Murphy 1973), impulsive oscillation of a cylinder (Stevenson 1973), and free motion of a displaced solid (Larsen 1969) and fluid sphere (McLaren *et al.* 1973), have been investigated. By contrast, numerical studies have considered the generation of internal waves by an oscillating bluff rectangular body (Liu 1989) and streamlined bodies (Nicolaou 1987).

Mowbray & Rarity (1967) considered the far-field wave system. Their shadowgraph and schlieren photographs of the phase configuration of the waves in a uniformly stratified fluid confirmed the fundamental results of the linear theory. Their inviscid and linear analysis showed that when a localized source oscillated with a fixed frequency ω in a stably stratified fluid of constant buoyancy frequency N, it generated an internal wave system forming a cross-wave in a vertical plane which radiated energy along cross-arms (rays) into the fluid. The rays had constant width and were inclined to the horizontal at the angle $\theta = \arcsin(\omega/N)$. These experiments are of general interest because they illustrated that the group and phase velocities of internal waves were perpendicular. Hurley (1969) found explicit solutions for slender cylinders having arbitrary cross-sections and demonstrated that one quarter of the power was radiated in each of four directions.

The inviscid analysis led to the result that the arms of the energy propagation had a constant width, but experiments showed that the arms widened with distance from the body. The viscous similarity solutions found by Thomas & Stevenson (1972) for a stratified fluid with a constant buoyancy frequency showed that viscosity widened the arms of the cross-wave and attenuated the amplitude. Viscous effects on internal cross-waves have been further analysed by Law, Peat & Stevenson (1982) and Peters (1985). Good agreement was found between the results of these experiments and the linear theory of Thomas & Stevenson (1972). Gordon, Klement & Stevenson (1975) extended the theory to a fluid with a variable buoyancy frequency N. The variation in the background buoyancy frequency produced curvature in the cross-arms. Peat (1978) found a similarity solution for a viscous rotating stratified fluid and showed that the cross-arm widths increase with distance from the source and the disturbance decays in amplitude along the rays, similar to non-rotating fluid. Nicolaou, Liu & Stevenson (1993) investigated a shear flow with a variable buoyancy frequency N and demonstrated how the reflection at a caustic modified the waves which then developed into thermocline waves.

Liu (1989) studied flow in a theoretically infinite physical domain. However, in order to carry out the computation, it was necessary to have a finite computational domain. The remedy adopted was to confine the computation to a domain bounded by artificial or computational boundaries, which would be referred to as open boundaries. The boundary conditions were established to allow the waves generated in the interior of the computational domain to propagate out of the boundary with the least influence on the flow inside the boundary. Liu's (1989) prescription of the open boundary conditions was similar to that used by Hirt & Cook (1972). In addition, Liu (1989) found that the open boundary conditions used by Orlanski (1976), Han, Meng & Innis (1983) and Pyret (1981) tended to produce both very severe numerical reflections and instabilities in the Marker and Cell (MAC) numerical method.

https://doi.org/10.1017/S0022112000008594 Published online by Cambridge University Press

Appleby & Crighton (1987) studied waves generated by a pulsating sphere, an oscillating cylinder and an oscillating sphere. They found that the waves have the same angle of propagation and parallel unchanging wave fronts between characteristic surfaces tangent to the body, although with different wavelengths. Therefore, any localized source of energy can generate internal waves with such a structure. The present model uses a momentum source $F \sin \omega t f(x, y)$ to generate internal waves, where $f(x, y)$ represents the momentum source domain. Such an approach obviates the need to use boundary conditions for the rigid wall of the wave source.

1.1. *Internal wave–wave interactions*

Resonant triad interactions are a significant mechanism in energy transfer to other modes and have been widely investigated. A triad interaction of internal waves redistributes energy and momentum among different wave components. According to weak interaction theory, the conditions for a resonant triad interaction are that (Phillips 1966)

$$K_2 \pm K_3 = K_1, \quad \omega_2 \pm \omega_3 = \omega_1, \tag{1.1}$$

and that all frequencies satisfy the dispersion relation $\omega_i = \Omega_i(K_i)$, where $K_i = (k_x, k_y, k_z)_i$ is the wavenumber vector and ω_i is the wave frequency.

The concept of nonlinear resonant interaction in a fluid dynamical context was introduced by Phillips (1960). Hasselmann (1962, 1966) derived a general wave–wave resonance theory of a continuous homogeneous weakly interacting random wave field. Bretherton (1964) investigated a mathematical basis for resonant interaction using a one-dimensional model equation. Davis & Acrivos (1967) first demonstrated the importance of nonlinear resonant interactions in inducing internal wave instabilities. Simmons (1969) simplified the interaction equations for weak, resonant wave interactions by slowly modulating the wave amplitude and phase angle, keeping frequency and wavenumber constant. Martin, Simmons & Wunsch (1972) were able to generate as many as five resonant triads from a single primary internal wave, each triad having the original internal wave included, leading them to conclude that resonant triad interactions are an important mechanism for transferring energy from a driving frequency to higher frequencies. McEwan (1973) crossed two beams of internal waves of different amplitude and frequency. The intense density gradients, or traumata, which preceded turbulence, were found to be due to strong nonlinearity in isopycnal distortion. Thorpe (1987*b*) considered resonant triad interaction of incident and reflected waves at a uniform slope and showed that nonlinear second- and third-order resonances occurred between incident and reflected waves, leading to regions of static instability off the slope.

The interaction of two internal wave rays has been studied theoretically by Kistovich & Chashechkin (1991) and experimentally by Chashechkin & Neklyudov (1990). Their spectral analysis indicated that the signals within the interaction region contained not only components at the original frequencies ω_1 and ω_2, but also at the difference frequency $|\omega_1 - \omega_2|$ and at the combination frequencies $2\omega_1 - \omega_2$, $2\omega_2 - \omega_1$, $3\omega_1 - 2\omega_2$ and so on.

Nonlinear non-resonant interactions have received little attention, even though they can transfer energy to frequencies higher than the buoyancy frequency. Therefore, the aim of this paper is to show that two intersecting beams of internal waves can transfer energy to the multiples, the divisions and the differences of the forcing frequencies, and also to show that the density field within the interaction region becomes unstable by transferring energy to standing higher evanescent modes rather

https://doi.org/10.1017/S0022112000008594 Published online by Cambridge University Press

than by resonant triad interaction. The effects of nonlinearity on the generation, propagation and reflection of internal waves also described in this study are used to choose the optimum parameters for the nonlinear model.

The governing equations for this study were solved using a SIMPLE scheme (Patankar 1980) on a non-staggered grid using a two-dimensional finite volume method (Armfield 1991, 1994) with open boundary conditions based on a Sommerfield radiation condition. The code was validated and a good energy balance was obtained. Lin *et al.* (1993) and Lombard & Riley (1994) pointed out that the instability that leads to wave overturning could be three-dimensional. Therefore, this two-dimensional model focuses strongly on the initiation of the wave overturning and the results reveal the fundamentals of the instability.

2. Governing equations and numerical model

The conservation equations of momentum, mass and volume are expressed in Euclidean coordinates (x, y) with corresponding velocity components (u, v) as follows:

$$\frac{\partial u}{\partial t} + u\frac{\partial u}{\partial x} + v\frac{\partial u}{\partial y} = -\frac{1}{\rho_o}\frac{\partial p}{\partial x} + \nu\nabla^2 u, \tag{2.1}$$

$$\frac{\partial v}{\partial t} + u\frac{\partial v}{\partial x} + v\frac{\partial v}{\partial y} = -\frac{1}{\rho_o}\frac{\partial p}{\partial y} - \frac{\rho}{\rho_o}g + \nu\nabla^2 v + F\sin(\omega t)(f_1(x,y) + f_2(x,y)), \tag{2.2}$$

$$\frac{\partial \rho}{\partial t} + u\frac{\partial \rho}{\partial x} + v\frac{\partial \rho}{\partial y} + v\frac{\mathrm{d}\hat{\rho}}{\mathrm{d}y} = \kappa\nabla^2\rho, \tag{2.3}$$

$$\frac{\partial u}{\partial x} + \frac{\partial v}{\partial y} = 0, \tag{2.4}$$

where t is the time, ρ, $\hat{\rho}$ and ρ_o are the fluctuating, background and reference densities respectively, ν is the coefficient of kinematic viscosity, κ is the coefficient of molecular diffusivity, $Ff_1(x, y)\sin\omega t$ and $Ff_2(x, y)\sin\omega t$ are the momentum sources used to generate two internal wave beams, F is the amplitude of the momentum sources, ω is the frequency of the momentum sources and $f_i(x, y)$ are the localization functions given by

$$f_i(x,y) = \begin{cases} \cos k_x(x - X_i)\exp(-300|k_x(y - Y_i)|^3) & \text{if } k_x|x - X_i| \leqslant 3\pi/2 \\ 0 & \text{otherwise,} \end{cases} \tag{2.5}$$

in which k_x is the horizontal wavenumber of the standing-wave-like momentum source and X_i and Y_i are the horizontal and vertical locations of the momentum sources respectively. The localization function imposes a standing-wave-like momentum source with a horizontal wavenumber of k_x and amplitude of $\exp(-300|k_x(y - Y_i)|^3)$. Because, the superposition of four pairs of travelling waves with frequency ω and $-\omega$, and wavenumber vectors (k_x, k_y), $(-k_x, k_y)$, $(k_x, -k_y)$ and $(-k_x, -k_y)$ can yield this standing wave, it can be expected that this momentum source will generate those travelling waves. The vertical wavenumber can be estimated by using the linear dispersion relation:

$$k_y = k_x\sqrt{N^2/\omega^2 - 1}. \tag{2.6}$$

https://doi.org/10.1017/S0022112000008594 Published online by Cambridge University Press

In order to scale the equations we introduce a characteristic time scale ω^{-1} and length scale k_x^{-1} and define non-dimensional variables as follows:

$$u' = \frac{u}{F/\omega}, \quad v' = \frac{v}{F/\omega}, \quad x' = \frac{x}{k_x^{-1}}, \quad y' = \frac{y}{k_x^{-1}},$$

$$t' = \frac{t}{\omega^{-1}}, \quad \rho' = \frac{\rho}{(\rho_o F/g)}, \quad p' = \frac{p}{\rho_o F k_x^{-1}}.$$

Substituting these variables into (2.1) to (2.4) and dropping the primes, we obtain the following non-dimensional equations:

$$\frac{\partial u}{\partial t} + Ke\left[u\frac{\partial u}{\partial x} + v\frac{\partial u}{\partial y}\right] = -\frac{\partial p}{\partial x} + Re^{-1}\nabla^2 u, \tag{2.7}$$

$$\frac{\partial v}{\partial t} + Ke\left[u\frac{\partial v}{\partial x} + v\frac{\partial v}{\partial y}\right] = -\frac{\partial p}{\partial y} - \rho + Re^{-1}\nabla^2 v + \sin(t)(f_1(x,y) + f_2(x,y)), \tag{2.8}$$

$$\frac{\partial \rho}{\partial t} + Ke\left[u\frac{\partial \rho}{\partial x} + v\frac{\partial \rho}{\partial y}\right] = Ri_m v + Re^{-1}Pr^{-1}\nabla^2\rho, \tag{2.9}$$

$$\frac{\partial u}{\partial x} + \frac{\partial v}{\partial y} = 0, \tag{2.10}$$

where

$$\left.\begin{aligned} Ri_m = \frac{(-g/\rho_o)(\mathrm{d}\hat{\rho}/\mathrm{d}y)}{\omega^2} = \left[\frac{N}{\omega}\right]^2, \quad Ke = \frac{Fk_x}{\omega^2}, \\ Pr = \frac{\nu}{\kappa}, \quad Re = \frac{\omega}{k_x^2\nu}, \quad \nabla^2 = \frac{\partial^2}{\partial x^2} + \frac{\partial^2}{\partial y^2}, \end{aligned}\right\} \tag{2.11}$$

and where $N = (g/\rho_o|\mathrm{d}\hat{\rho}/\mathrm{d}y|)^{1/2}$ is the buoyancy frequency. The Keulegan number Ke represents the ratio of the period of oscillation to the time taken for an eddy to roll up. Therefore, for large Keulegan numbers the period of oscillation is large compared to the time taken for eddies to roll up implying the importance of the advective acceleration terms. By contrast, the Reynolds number is the ratio of the time scales: $1/k_x^2\nu$ and ω^{-1}.

The study of waves in isolation requires an open boundary to allow waves to freely propagate through the boundary. Simple extrapolation formulae, Newtonian and viscous damping, one-sided differencing methods and the Sommerfield radiation condition have been developed to satisfy this requirement. The Sommerfield radiation condition has been used widely in theoretical studies because the dispersion characteristics of the waves are then known. Using this approach, to ensure waves propagate unchanged, it is necessary to specify at the boundary (Han *et al.* 1983)

$$\frac{\partial \phi}{\partial t} + c\frac{\partial \phi}{\partial x} = 0, \tag{2.12}$$

where ϕ is any flow variable and c is the local phase speed of the waves. If ϕ is expressed as a two-dimensional plane wave

$$\phi = \phi_o \mathrm{e}^{\mathrm{i}(k_x x + k_y y - \omega t)}, \tag{2.13}$$

https://doi.org/10.1017/S0022112000008594 Published online by Cambridge University Press

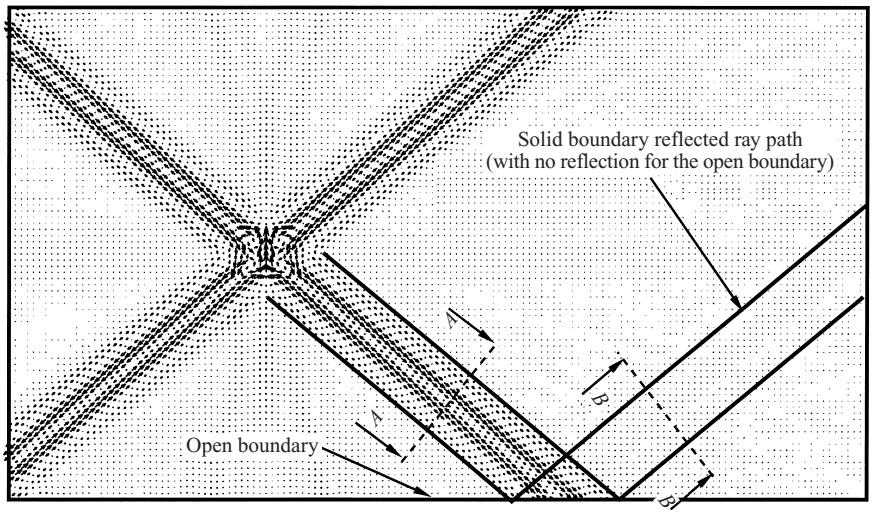


FIGURE 1. The configuration used to estimate the reflection coefficient from the open boundary.

the following relationships are valid:

$$\frac{\partial \phi}{\partial t} + c_x \frac{\partial \phi}{\partial x} = 0, \quad \frac{\partial \phi}{\partial t} + c_y \frac{\partial \phi}{\partial y} = 0, \tag{2.14}$$

where $c_x = \omega/k_x$ and $c_y = \omega/k_y$. No reflection takes place with this boundary condition, provided the propagation speed c in (2.12) is the component normal to the boundary.

This formulation requires nonlinear advective transport effects to be absent and the waves to be locally planar, giving each point a unique phase speed. As the small scales in this study are contained in the interaction region and do not propagate to the boundaries, it is thus unnecessary to have a scheme that allows for the passage of higher harmonics. In addition, Ke was reduced in the near boundary region to ensure that the waves at the boundary were at most only weakly nonlinear. Different size domains were used to ensure that the boundary conditions did not influence the solution. Additionally, in order to evaluate the reflection from the open boundary we conducted a few simulations for different degrees of nonlinearity ($Ke = 0.025$, 0.05, 0.1, 0.2, 0.3 and 0.4). The Reynolds, Prandtl and model Richardson numbers were kept at $Re = 25\,000$, $Pr = 7$ and $Ri_m = 2.5$, respectively. The computational domain consisted of 161×281 uniform cells with non-dimensional size of $\Delta x = \Delta y = 2\pi/20$. A time step of $2\pi/2000$ was chosen and the momentum source was located at $(0.3L_x, 0.5L_y)$ where the L_x and L_y are the length and width of the computational domain, respectively. The reflection coefficient, which was defined as the ratio of the energy flux density of the waves inside the boundary to that of the incident waves (figure 1), was increased from 0.3% for Keulegan numbers of less than 0.2 to 0.9% at $Ke = 0.4$ (figure 2). Therefore, in our simulations, the Keulegan number was limited to less than $Ke = 0.4$ to ensure that the reflected waves had only a minor influence on the solution. The radiation condition given above may only be used for locally plane waves with outward normal group velocity. The use of a relatively peaked wavenumber source term ensures that this boundary condition performs well here.

https://doi.org/10.1017/S0022112000008594 Published online by Cambridge University Press

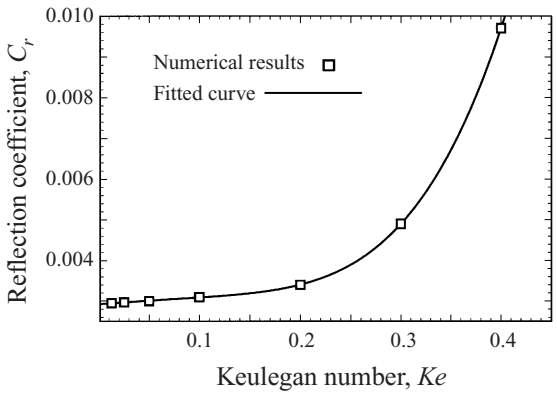


FIGURE 2. Reflection coefficient plot for the different Keulegan numbers. The reflected energy flux density from the open boundary is less than 1% for the simulated cases.

Reynolds number	25 000	25 000	25 000	25 000	10 000	4000	1600
Keulegan number	0.1	0.05	0.025	0.0125	0.0125	0.0125	0.0125
Ray width $l_r/2\pi$	0.70	0.70	0.70	0.70	0.76	0.82	0.89
Wave amplitude ζ	0.51	0.51	0.51	0.51	0.49	0.39	0.25
Angle of propagation (deg.)	45	45	45	45	45	45	45

TABLE 1. Wavelength at the equal distance from the momentum source for different Reynolds and Keulegan numbers.

3. Discussion

3.1. *The effects of viscosity and nonlinearity on the generation and propagation of internal waves*

Results are presented for a computational domain of 132×132 uniform cells with non-dimensional size $\Delta x = \Delta y = 0.12\pi$ and a time step of $\Delta t = 2\pi/1000$. A single momentum source (e.g. $f_2(x, y) = 0$) was located at the centre of the domain. Because a third-order QUICK scheme can lead to a numerically dissipative system, a grid dependence test was carried out. Theoretically the dissipation associated with such a QUICK scheme is $Keu\,\Delta x^3/24$, which for this flow and mesh was typically less than one eighth of the molecular diffusion. Similar tests were carried out to ensure time step independence. We also conducted tests on domains of different sizes to ensure that the boundary conditions did not influence the solution in the interior of the domain.

To determine the effect of viscosity, simulations were performed using different Reynolds numbers. The non-dimensional parameters were chosen as follows: $Pr = 7$, $Ri_m = 2$, $Re = 25\,000$, 10 000, 4000 and 1600, and $Ke = 0.0125$. The simulations were performed for eleven wave periods (T) and the results for the highest and lowest Reynolds numbers are presented in figure 3. Waveforms at cross-section AA are shown at the top of each plot; the horizontal and vertical axes are in terms of the non-dimensional length and velocity scale, respectively. The ray width l_r and wave amplitude ζ along the cross-section AA for the Reynolds and Keulegan numbers range simulated are given in table 1; the width increased and amplitude decreased with decreasing Reynolds number and increasing distance from the source. The numerical

https://doi.org/10.1017/S0022112000008594 Published online by Cambridge University Press

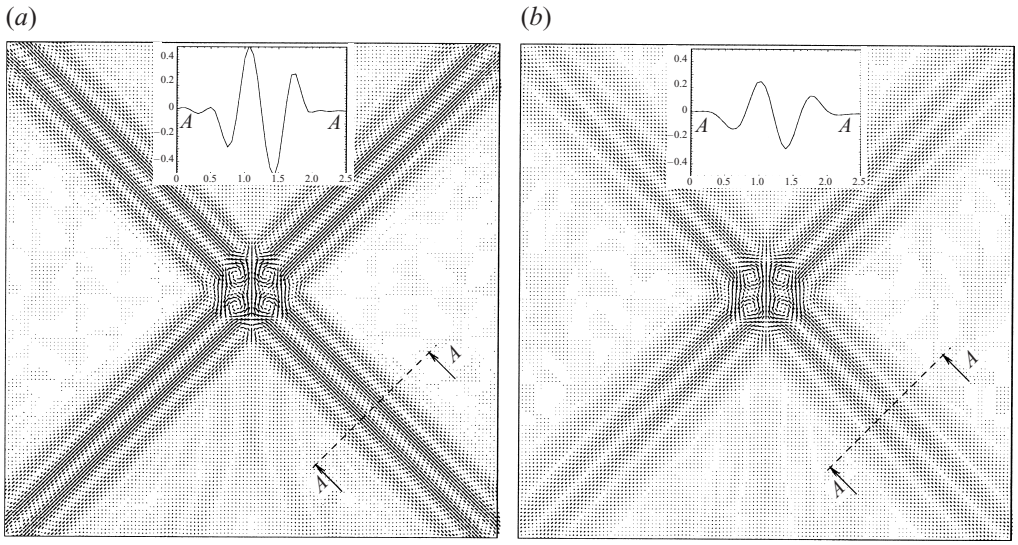


FIGURE 3. Velocity vectors and velocity contour plots for the internal wave, $Ri_m = 2$, $Ke = 0.0125$, $Pr = 7$. The Reynolds numbers are (*a*) 25 000 (*b*) 1600. The ray width decreases as the Reynolds number increases. The ray width is defined as the distance between the first zero crossings on either side of the ray centre.

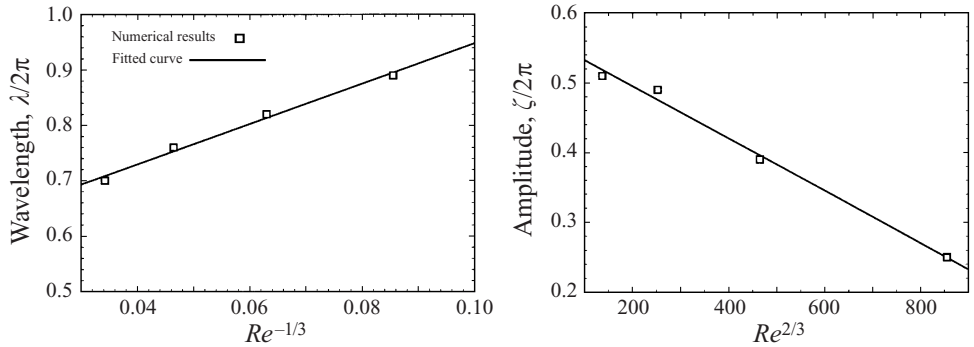


FIGURE 4. The wavelength and wave amplitude variation with Reynolds number *Re*. The wave width decreases and wave amplitude increases as the Reynolds number increases.

results confirm, as shown in figure 4, the relationship first established by Thomas & Stevenson (1972):

$$l_r/2\pi = 0.584 + 3.647 \times Re^{-1/3}, \tag{3.1}$$

$$\zeta/2\pi = 0.570 - 3.75 \times 10^{-4} \times Re^{2/3}. \tag{3.2}$$

The influence of the nonlinear advective terms was investigated by carrying out simulations for the range of Keulegan numbers: $Ke = 0.1, 0.05, 0.025$ and 0.0125 and a large Reynolds number of 25 000 (Pr and Ri_m are the same as in the previous simulations). The results were insensitive to such small changes of the Keulegan number and all were similar to the previous results for that Reynolds number (table 1).

In order to obtain higher Keulegan numbers and greater nonlinearity, the Reynolds number was reduced to 5000. Figure 5 contains the velocity vector plots for $Ke = 0.1$,

https://doi.org/10.1017/S0022112000008594 Published online by Cambridge University Press

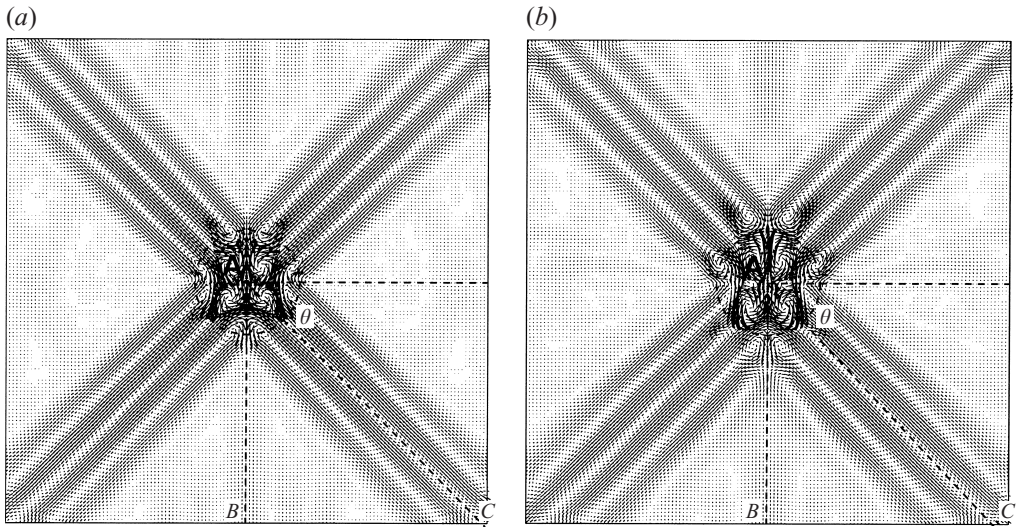


FIGURE 5. Velocity vector plots for the internal wave, $Ri_m = 2$, $Re = 5000$, $Pr = 7$. The Keulegan numbers are (*a*) 0.1, (*b*) 0.4. The angle of the ray to the horizontal increases as the nonlinearity becomes stronger.

Keulegan number	0.1	0.2	0.3	0.4
$BC/2\pi$	3.88	3.80	3.72	3.64
$AB/2\pi$	3.96	3.96	3.96	3.96
$\tan\theta = AB/BC$	1.021	1.042	1.064	1.087
θ (deg.)	45.60	46.18	46.78	47.40

TABLE 2. The angle of the ray to the horizontal for different Keulegan numbers.

and 0.4. The Pr and Ri_m were the same as in the previous simulations. Table 2 indicates that the angle to the horizontal increases slightly (about 2°) with increasing Keulegan number, which implies that the effective vertical wavenumber is increased slightly, but the horizontal wavelength remained unchanged. The small decrease in wave amplitude with increasing Keulegan number is probably due to less efficient wave generation of the source.

3.2. *Symmetric and non-symmetric wave–wave interaction*

The spatial domain was discretized with 240×160 uniform cells leading to a non-dimensional mesh size of $\Delta x = \Delta y = 2\pi/20$. The parameter values were: $Re = 25\,000$, $Ke = 0.1$, 0.375, $Ri_m = 2.5$, $Pr = 7$. The two momentum sources were located at $(0.35L_x, 0.50L_y)$ and $(0.65L_x, 0.50L_y)$ (figure 6). Velocity vector plots are shown in figure 6 for $Ke = 0.1$, ten wave periods after start up. The rays generated travelled out from the sources and the wave energy was transported along the ray path at the group velocity. The rays intersected in two interaction regions (figure 6); only the results from the lower interaction region are presented here.

In order to understand the interaction in the overturn region, it is useful to first discuss the flow field. Figures 7 and 8 contain a sequence of plots depicting the evolution of the wave interaction with time T, where the time is in wave periods ($T = t/2\pi$). The velocity field is indicated by vectors, the density field by contour

https://doi.org/10.1017/S0022112000008594 Published online by Cambridge University Press

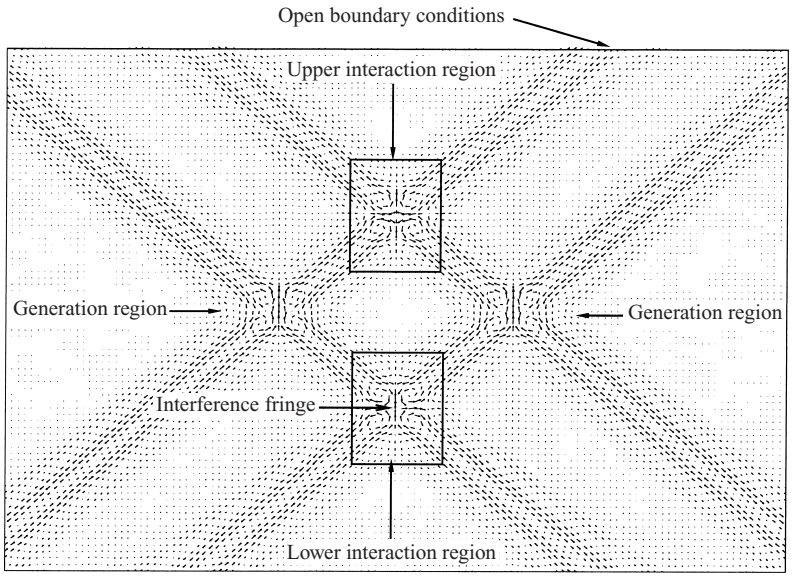


FIGURE 6. Velocity vector plots on every second grid point for the internal wave, $Ri_m = 2.5$, $Ke = 0.1$, $Pr = 7$ and $Re = 25\,000$, at time $T = 10$. Two momentum sources are used to generate internal waves.

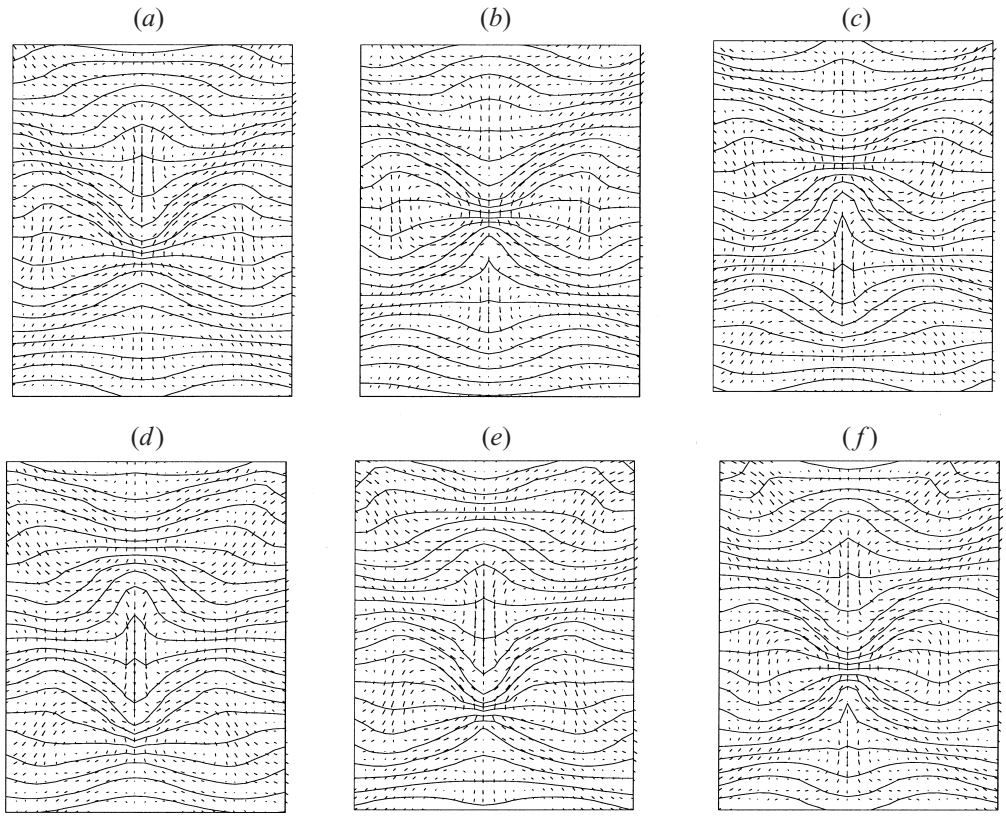


FIGURE 7. Velocity vectors and density contours, $Ri_m = 2.5$, $Ke = 0.375$, $Pr = 7$ and $Re = 25\,000$. Times are (*a*) 5, (*b*) 5.2, (*c*) 5.4, (*d*) 5.6, (*e*) 5.8 and (*f*) 6. Stagnation points propagate vertically upwards within the intersection region.

https://doi.org/10.1017/S0022112000008594 Published online by Cambridge University Press

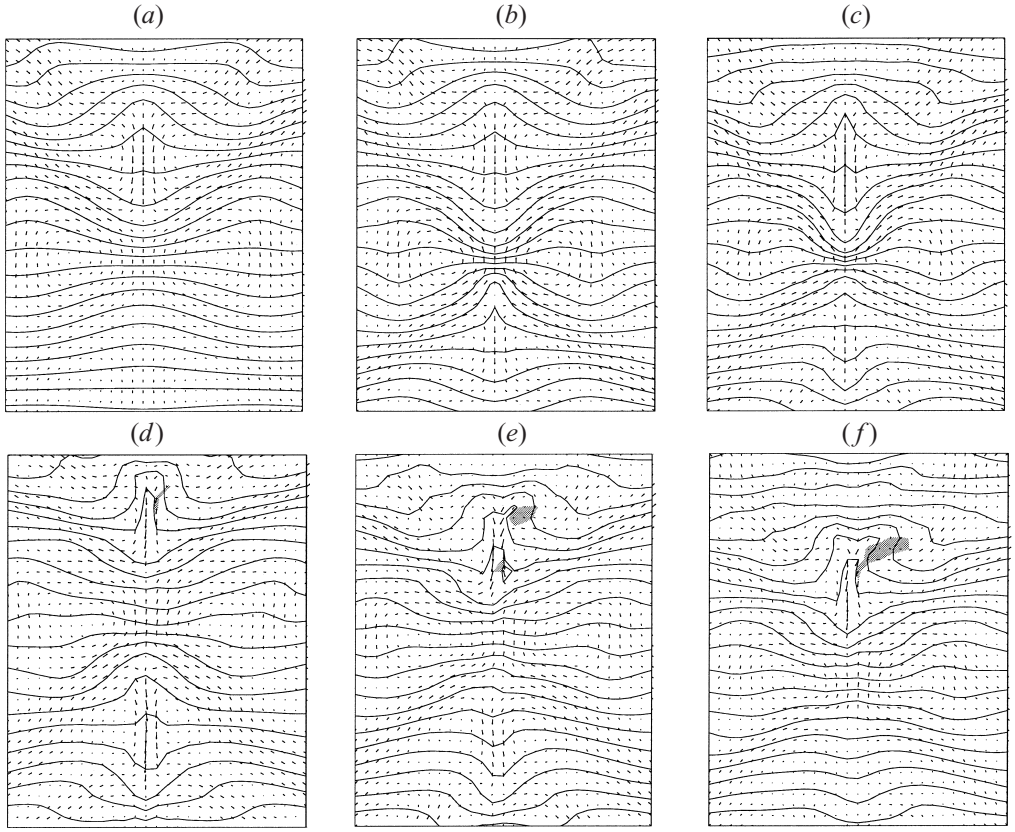


FIGURE 8. Velocity vectors and density contours, $Ri_m = 2.5$, $Ke = 0.375$, $Pr = 7$ and $Re = 25\,000$. Shading indicates regions of density overturning. Times are (*a*) 4, (*b*) 6, (*c*) 8, (*d*) 10.2, (*e*) 11.1 and (*f*) 11.9. Density overturning occurs when the wave has reached a high amplitude.

lines, and shading is used to indicate regions of density overturning (i.e. where $\mathrm{d}(\rho + \hat{\rho})/\mathrm{d}y \geqslant 0$).

The linear superposition of two plane monochromatic waves of identical properties but opposite horizontal phase velocities

$$\exp\left[\mathrm{i}(k_x x + k_y y - \omega t)\right] + \exp\left[\mathrm{i}(-k_x x + k_y y - \omega t)\right] \tag{3.3}$$

yields a modulated plane wave

$$2\cos\left(k_x x\right)\exp\left[\mathrm{i}(k_y y - \omega t)\right], \tag{3.4}$$

the cosine amplitude modulation accounting for interference fringes. The velocity field exhibits stagnation points on the nodes of interference fringes (figure 6) propagating vertically upwards within the intersection region (figure 7).

The plots also indicate that the amplitude of the resultant wave, which propagates vertically within the interaction region, increases with time until a density overturning occurs. The first instability became visible at time $T = 10.2$. Prior to this time, the internal wave field was symmetrical about the vertical centreline of the interaction region, indicating that the flow region was basically two-dimensional while it remained stable (figure 8). With the overturning of the waves symmetry is lost (figure 8*d*) and

https://doi.org/10.1017/S0022112000008594 Published online by Cambridge University Press

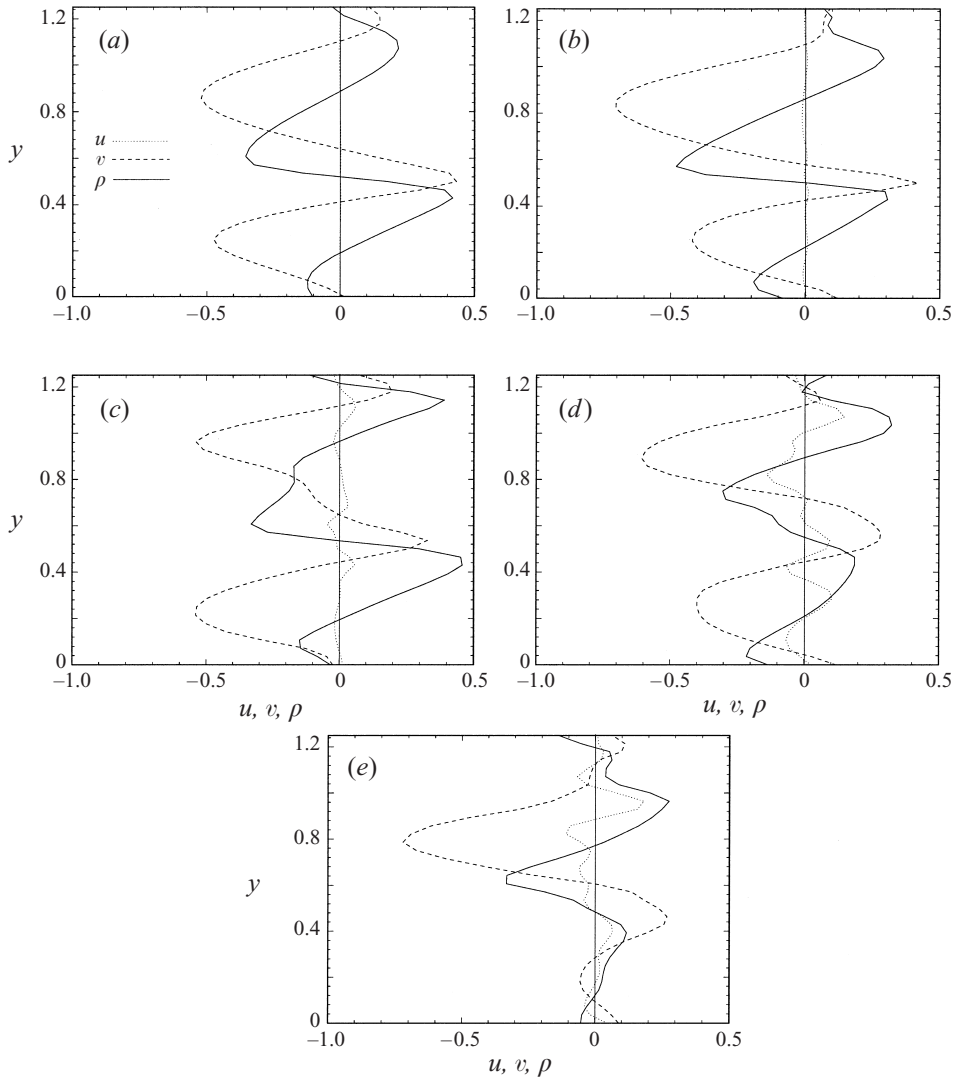


FIGURE 9. Horizontal and vertical velocities and density fluctuations along the centreline of the interaction region, $Ri_m = 2.5$, $Ke = 0.375$, $Pr = 7$ and $Re = 25\,000$. Times are (*a*) 6.0, (*b*) 8.0, (*c*) 10.0, (*d*) 11.0 and (*e*) 12.0. Phase difference between the density and velocity fluctuations changes with the presence of the higher modes.

the flow becomes three-dimensional (Lin *et al.* 1993; Lombard & Riley 1994). This means that a two-dimensional model is sufficient to study the mechanism of the superharmonic instability; however, a three-dimensional model is needed to investigate the small scales produced by overturning and also to study the other possible unstable modes with variation in the third dimension.

Horizontal and vertical velocities and density fluctuations along the centreline of the interaction region are plotted in figure 9. The phase difference between the density and vertical velocity fluctuations is $\pi/2$, as predicted by linear theory (Phillips 1966). This phase difference was distorted by the emergence of the smaller scales which also

https://doi.org/10.1017/S0022112000008594 Published online by Cambridge University Press

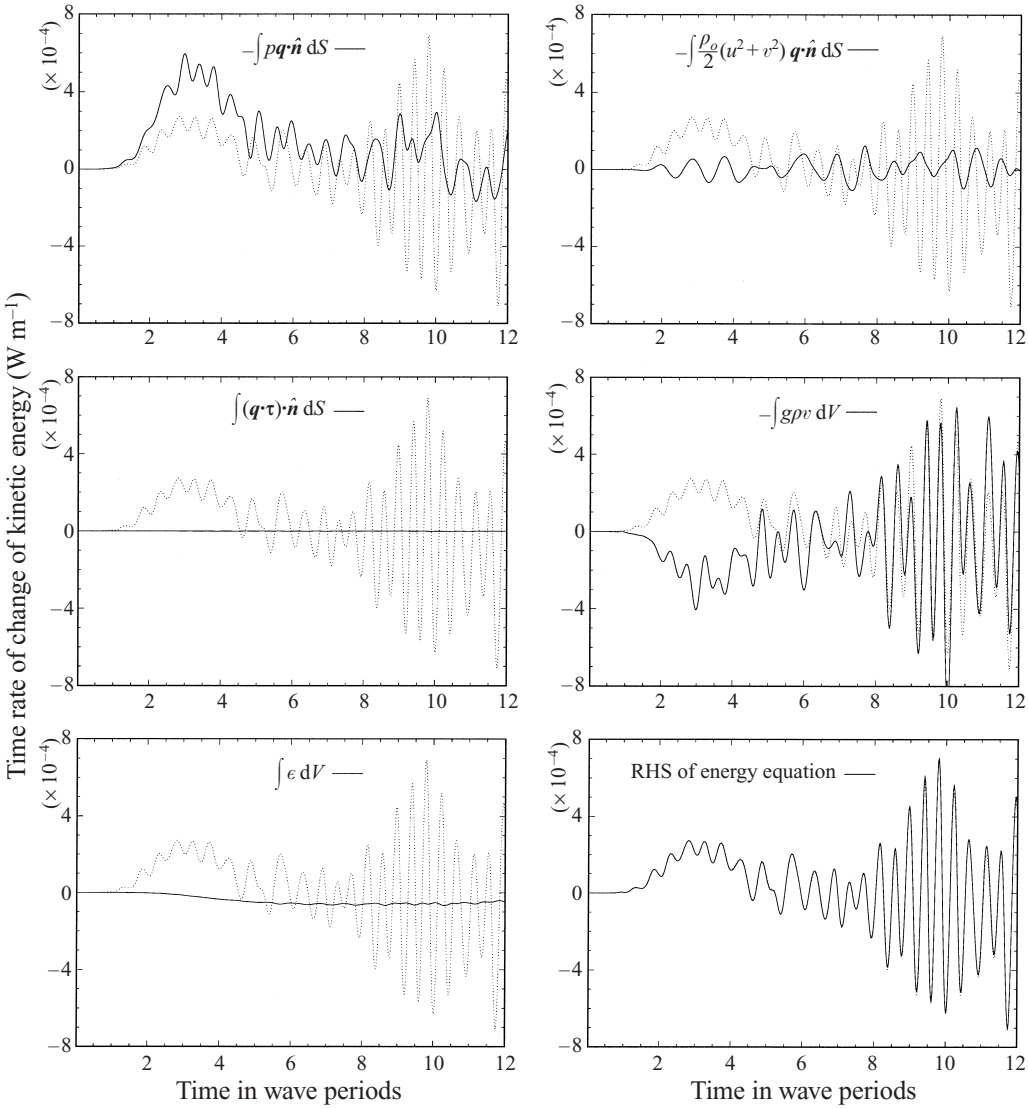


FIGURE 10. Time series of each term in the energy equation (3.6), $Ri_m = 2.5$, $Ke = 0.375$, $Pr = 7$ and $Re = 25\,000$. The higher modes develop from about $T = 5.5$. Dotted line is the total.

exhibited horizontal velocity fluctuations (figure 9*b*); smaller scales are clearly shown in figures 9*b*, 9*c* and 9*d*.

Within a fixed volume V, the perturbation kinetic energy E_k is defined as

$$E_k = \frac{\rho_o}{2}\int_V q^2\,\mathrm{d}V, \tag{3.5}$$

where $\boldsymbol{q} = (u, v)$. An equation for the time rate of change of the kinetic energy can be obtained from the dimensional form of (2.7) and (2.8) (see e.g. Landau & Lifshitz 1987):

$$\frac{\mathrm{d}E_k}{\mathrm{d}t} = -\oint_S \left[p\boldsymbol{q} + \frac{\rho_o}{2}q^2\boldsymbol{q} - \boldsymbol{q}\cdot\boldsymbol{\tau}\right]\cdot\hat{\boldsymbol{n}}\,\mathrm{d}S - \int_V g\rho v\,\mathrm{d}V - \int_V \epsilon\,\mathrm{d}V, \tag{3.6}$$

https://doi.org/10.1017/S0022112000008594 Published online by Cambridge University Press

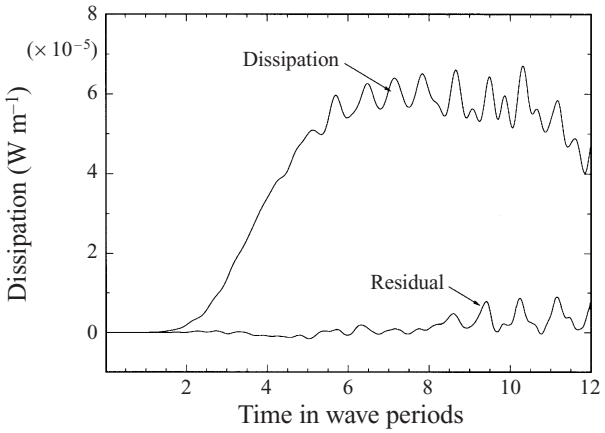


FIGURE 11. Comparison of the dissipation with the residual of the energy equation, $Ri_m = 2.5$, $Ke = 0.375$, $Pr = 7$ and $Re = 25\,000$. Because the computational grid size is much larger than the Kolmogorov scale, the estimated dissipation is expected to be less than the actual value.

where $\boldsymbol{q} \cdot \boldsymbol{\tau}$ is the vector with components $u_i \tau_{ij}$, τ_{ij} are the elements of the viscous stress tensor $\boldsymbol{\tau}$, $\hat{\boldsymbol{n}}$ denotes the unit vector normal to the surface S enclosing V, and the kinetic energy dissipation rate per unit volume ϵ is defined as

$$\epsilon = \tau_{ij} \frac{\partial u_i}{\partial x_j}. \tag{3.7}$$

The first term on the right-hand side of (3.6) is the rate change of kinetic energy resulting from pressure work, advection, and viscous diffusion of energy across the bounding surface S. The second term is the reversible rate of exchange with potential energy, while the third term is the irreversible rate of conversion from mechanical to internal energy through viscous dissipation. These terms are compared with the time rate of change of kinetic energy in figure 10. As the wave packets entered the interaction region ($T \simeq 1$), the kinetic energy, and all the other terms, began to increase in amplitude and the small spatial scales formed leading to a growth in dissipation. Between $T = 1$ and $T = 5.5$, the terms were purely periodic in time and the frequency of oscillations remained the same. Higher modes developed from about $T = 5.5$; these features are examined below using spectral analysis.

Because the QUICK scheme is dissipative it is important to verify that the numerical dissipation was less than the physical dissipation. To do this we computed the residual from the energy equation defined as

$$\text{Residual} = \frac{\mathrm{d}}{\mathrm{d}t}\left\{\frac{\rho_o}{2}\int_V q^2 \,\mathrm{d}V\right\} - \left\{-\oint_S \left[p\boldsymbol{q} + \frac{\rho_o}{2} q^2 \boldsymbol{q} - \boldsymbol{q} \cdot \boldsymbol{\tau}\right] \cdot \hat{\boldsymbol{n}} \,\mathrm{d}S - \int_V g\rho v \,\mathrm{d}V - \int_V \epsilon \,\mathrm{d}V\right\}. \tag{3.8}$$

From the curves shown in figure 11 it is clear that the numerical dissipation was only a small fraction ($< 16\%$) of the physical dissipation, the maximum being reached once small scales had formed.

Density fluctuation spectra for locations inside the incoming ray, inside the outgoing ray, and at three points inside the interaction region were used to examine the

https://doi.org/10.1017/S0022112000008594 Published online by Cambridge University Press

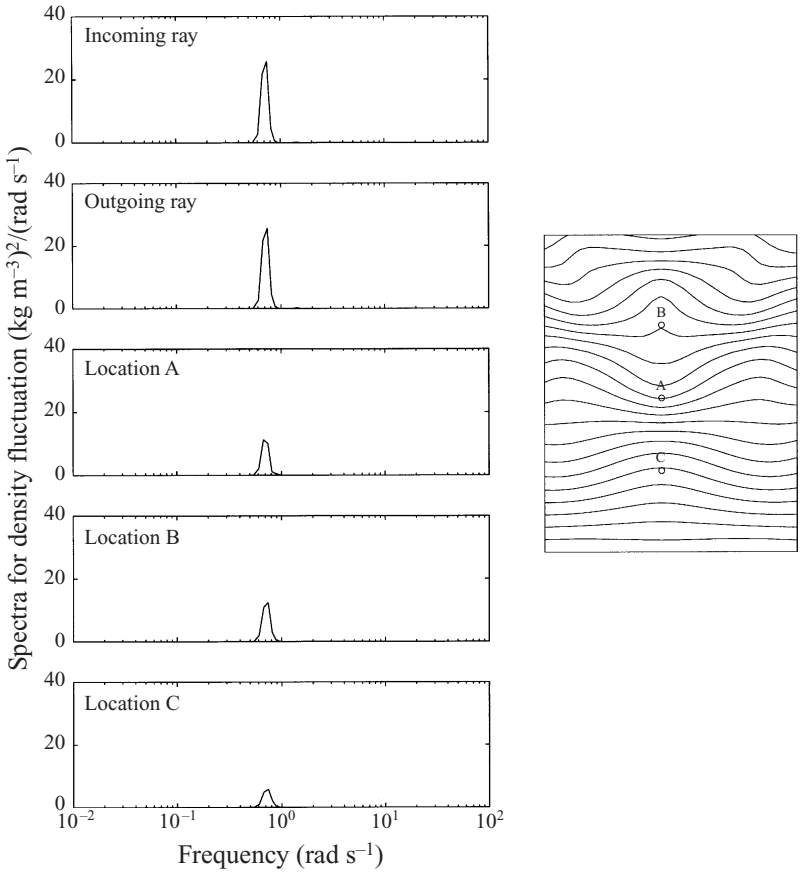


FIGURE 12. Spectra for density fluctuations, $Ri_m = 2.5$, $Ke = 0.1$, $Pr = 7$ and $Re = 25\,000$. The locations in the interaction region are shown at the right-hand side. The higher modes are not excited for the weakly nonlinear case.

mechanism of wave breaking inside the interaction region. The forcing frequency was 0.7 rad s^{-1} and spectra were obtained for $0 \leqslant T \leqslant 10$. Figure 12 indicates that for lower Keulegan numbers, modes within the interaction region have the forcing frequency and no excitation of modes is evident. However, for the larger Keulegan numbers (figure 13) modes with a frequency of 1.4 and 2.1 rad s^{-1} were excited (see also Teoh, Ivey & Imberger 1997 and Javam *et al.* 1995). Because these modes were absent in spectra for lower Keulegan numbers (figure 12) the excited modes must be due to nonlinear interaction. The frequencies of the excited modes were greater than the local buoyancy frequency (1.1 rad s^{-1}), and therefore the waves could not propagate outside the interaction region, leading to an accumulation of energy within the interaction region. The spectral energy inside the interaction region was higher than that in the incoming ray, and the energy in the outgoing ray showed a corresponding lower energy (figure 13).

Short-time Fourier distributions, for time interval $\Delta T = 2\pi/1600$, for density fluctuations at the locations A, B, and C illustrate that the higher modes developed after time $T = 5.5$ (figure 14). It is interesting to note that the smaller length scales formed at the time when the waves started to intersect (figure 15), whereas the higher

https://doi.org/10.1017/S0022112000008594 Published online by Cambridge University Press

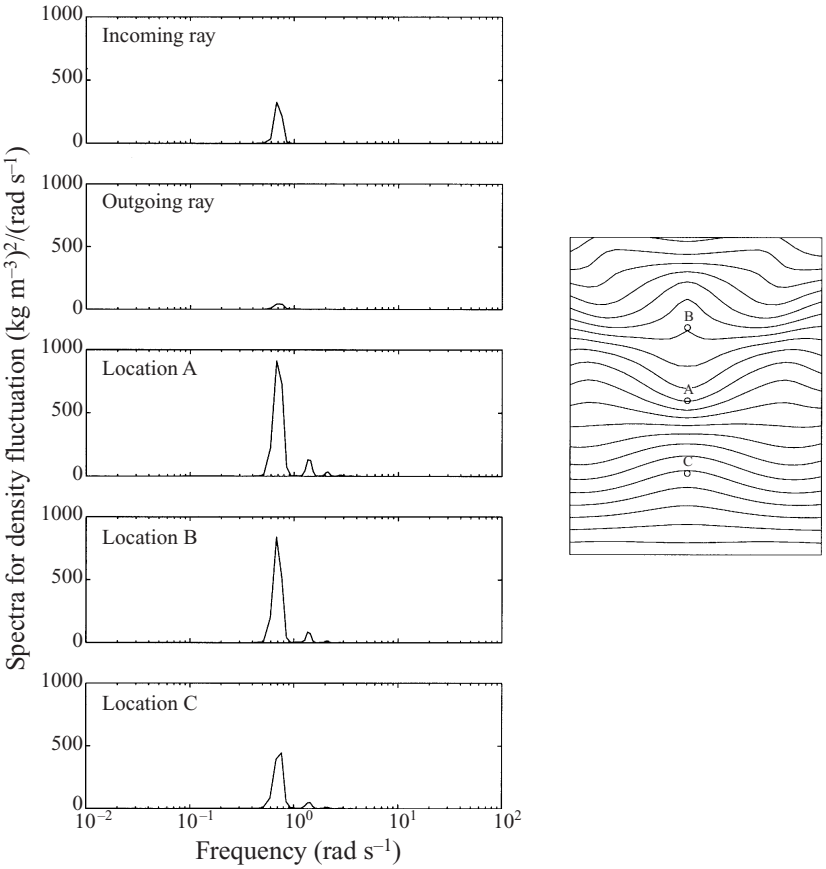


FIGURE 13. Spectra for density fluctuations computed from the time series collected within the rays for ten periods from the onset of the overturning, $Ri_m = 2.5$, $Ke = 0.375$, $Pr = 7$ and $Re = 25\,000$. The locations in the interaction region are shown at the right-hand side. The trapped energy excites higher modes.

harmonics developed a few periods later. A sequence of two-dimensional wavenumber spectra for the density fluctuations within the interaction region for the different times are shown in figure 15. The internal waves generated by the momentum sources have wavevectors of $(5/2\pi, 6/2\pi)$ and $(-5/2\pi, 6/2\pi)$. For the linear superposition of these two waves, the resultant wavevector is expected to be $(0, 6/2\pi)$ (equation (3.4)). However, the following wavenumbers are represented in figure 15:

$$k_x = 5/2\pi,\ 10/2\pi,\ 15/2\pi,\ 20/2\pi; \qquad k_y = 6/2\pi,\ 12/2\pi,\ 18/2\pi,\ 24/2\pi.$$

The excited higher modes and larger wavenumbers are multiples of the primary frequency ω and wavenumbers k_x, k_y (figures 13 and 15). Such modes do not satisfy the conditions for resonant triad interaction (equation (1.1)). In addition, because the spatial interaction developed much earlier than temporal interaction, a triad interaction could not have formed. In our case nonlinear interactions produced higher modes which were unable to propagate away as their frequencies were greater than the buoyancy frequency N; these modes were trapped in the interaction region.

https://doi.org/10.1017/S0022112000008594 Published online by Cambridge University Press

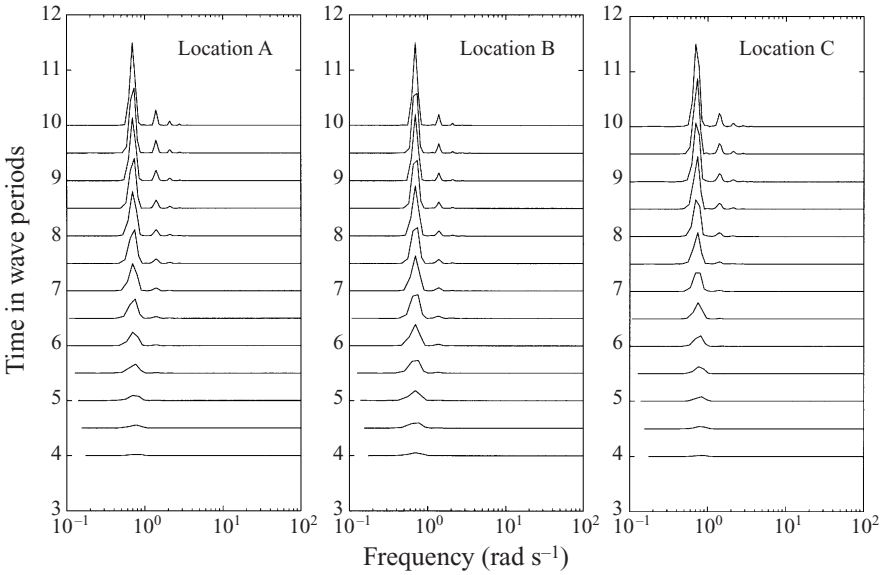


FIGURE 14. Short-time Fourier distribution for density fluctuations, $Ri_m = 2.5$, $Ke = 0.375$, $Pr = 7$ and $Re = 25\,000$. The higher modes develop at time $T = 5.5$.

The subsequent build up of energy associated with this trapping led to overturning. This mechanism was also demonstrated experimentally by Teoh *et al.* (1997).

A similar problem was studied experimentally by McEwan (1973). He showed that energy was transferred to subharmonics with half the forcing frequency and with a longer horizontal wavelength. The energy transfer was caused by the formation of a parametric subharmonic triad instability. However, experimental results of Teoh *et al.* (1997) and numerical simulations in this study show no sign of energy at this frequency; instead, energy was transferred to the evanescent modes. An explanation for the energy transfer to lower modes seen in McEwan's (1973) experiment was sought by conducting a numerical simulation of non-symmetric wave–wave interaction similar to his experiments.

For these simulations the computational domain consisted of 348×232 uniform cells with non-dimensional size of $\Delta x = \Delta y = 2\pi/20$ (figure 16). The dimensional scaling is as follows: $L = (\lambda_l + \lambda_r)/2$, $T = 2/(\omega_l + \omega_r)$ and $N = 1.025\,\mathrm{rad\,s^{-1}}$, where $\lambda_l = 30.5\,\mathrm{cm}$ and $\omega_l = 0.52\,\mathrm{rad\,s^{-1}}$ were wavelength and frequency of the left-hand-side momentum source and $\lambda_r = 16\,\mathrm{cm}$ and $\omega_r = 0.68\,\mathrm{rad\,s^{-1}}$ were wavelength and frequency of the right-hand-side momentum source. This choice resulted in $Ri_m = 4.18$, $Pr = 700$ and $Re = 32\,500$. Two cases were simulated, $Ke = 0.05$ and $Ke = 0.225$. The density fluctuation spectra for three locations within the interaction region are plotted in figure 17 for $Ke = 0.05$. No production of modes is visible within the interaction region. However, as seen in figure 18, for the larger Keulegan number $Ke = 0.225$ (nonlinear case) the multiples of the forcing frequencies (e.g. $2\omega_l = 1.04\,\mathrm{rad\,s^{-1}}$), divisions of the forcing frequencies including frequencies observed in McEwan's experiment (e.g. $\omega_l/2 = 0.26\,\mathrm{rad\,s^{-1}}$) and the combination of the difference frequencies (e.g. $\omega_r - \omega_l = 0.16\,\mathrm{rad\,s^{-1}}$, $2\omega_r - \omega_l = 0.84\,\mathrm{rad\,s^{-1}}$, $2\omega_l - \omega_r = 0.36\,\mathrm{rad\,s^{-1}}$, $3\omega_r - 2\omega_l = 1.0\,\mathrm{rad\,s^{-1}}$, $2(\omega_r - \omega_l) = 0.32\,\mathrm{rad\,s^{-1}}$ and $(3\omega_r - 2\omega_l)/2 = 0.50\,\mathrm{rad\,s^{-1}}$) were all excited (see also Kistovich & Chashechkin 1991 and Chashechkin & Neklyudov

https://doi.org/10.1017/S0022112000008594 Published online by Cambridge University Press

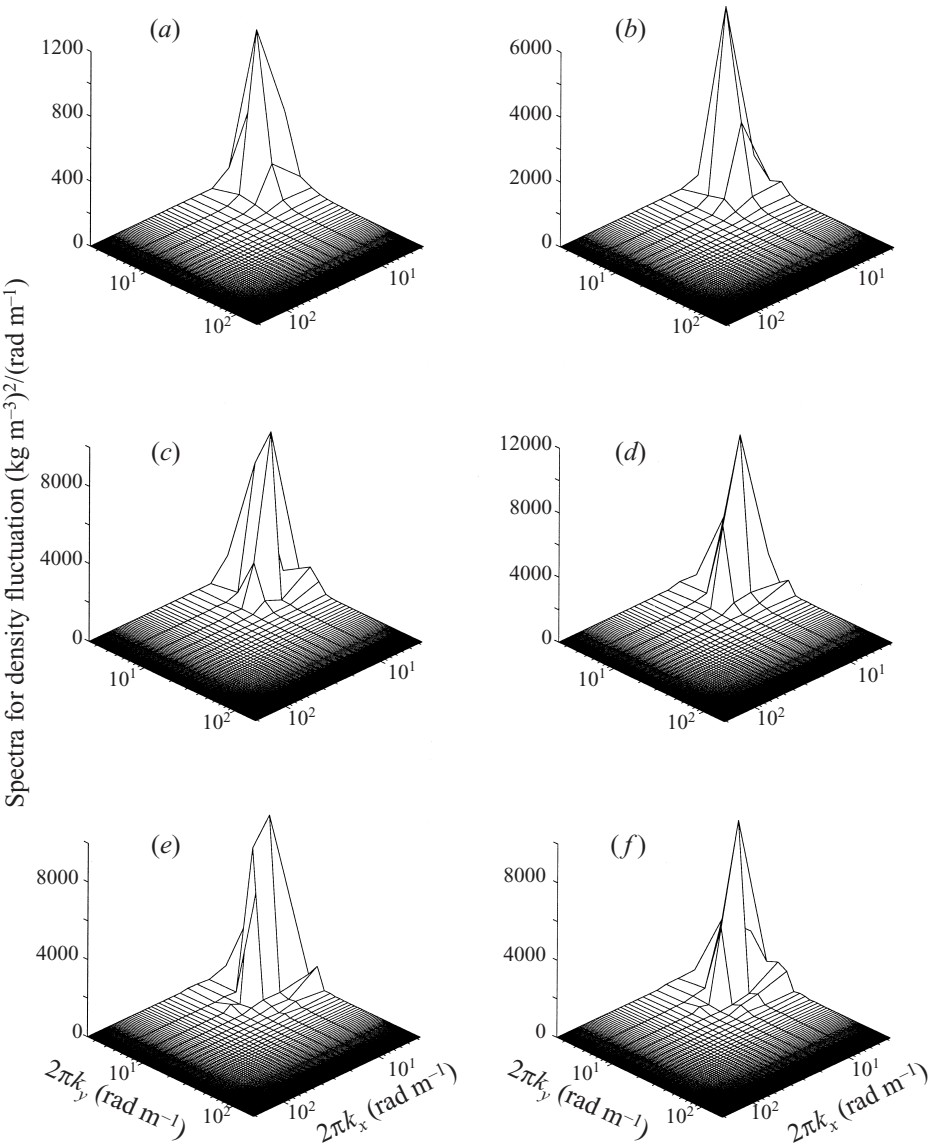


FIGURE 15. Two-dimensional wavenumber spectrum for the interaction region, $Ri_m = 2.5$, $Ke = 0.375$, $Pr = 7$ and $Re = 25\,000$. Times are (*a*) 2, (*b*) 3, (*c*) 4, (*d*) 5, (*e*) 6 and (*f*) 11. Smaller wavenumbers develop at the time when they start to intersect.

1990). It is therefore clear that transfer of energy to lower modes, as observed by McEwan (1973), only occurs for the non-symmetric case and cannot be expected in the experiments of Teoh *et al.* (1997).

Makarov, Neklyudov & Chashechkin (1990) proved that different types of velocity profiles are observed depending on the size of the source, buoyancy frequency and viscosity. These profiles have been referred to as 'unimodal' and 'bimodal'. Kistovich & Chashechkin (1991) and Chashechkin & Neklyudov (1990) proved that internal wave–wave interactions depend markedly on the internal structure of the beams.

https://doi.org/10.1017/S0022112000008594 Published online by Cambridge University Press

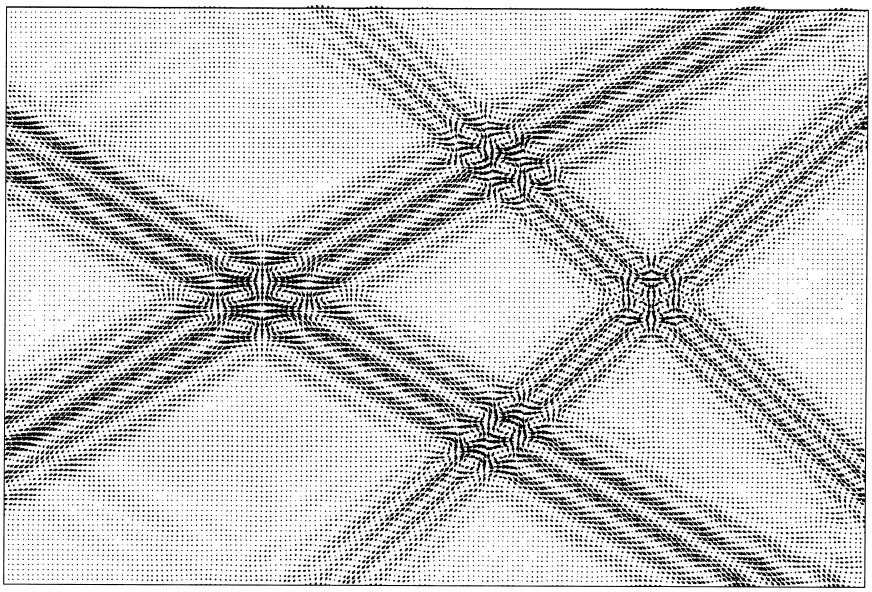


FIGURE 16. Velocity vector plots for the internal wave, $Ri_m = 4.18$, $Ke = 0.05$, $Pr = 700$ and $Re = 32\,500$; at time $T = 12$. Two non-symmetric momentum sources are used to generate internal waves.

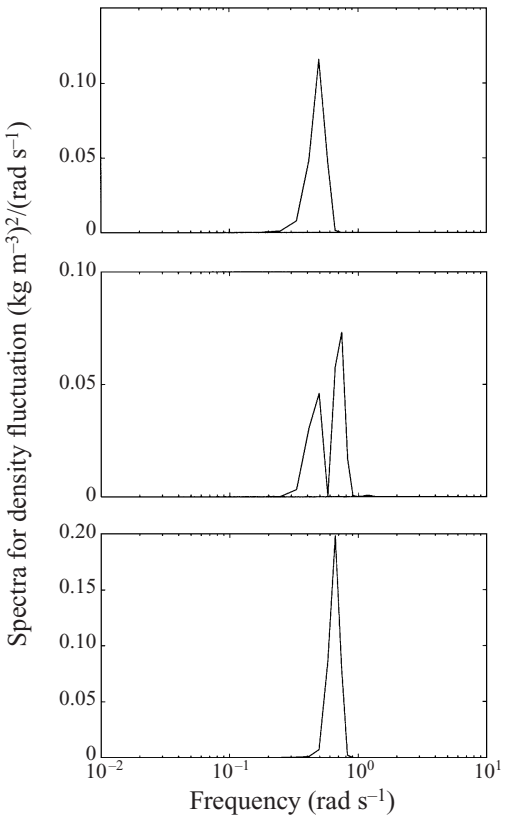


FIGURE 17. Spectra for density fluctuations at three locations within the interaction region, $Ri_m = 4.18$, $Ke = 0.05$, $Pr = 700$ and $Re = 32\,500$. Harmonics are not excited.

https://doi.org/10.1017/S0022112000008594 Published online by Cambridge University Press

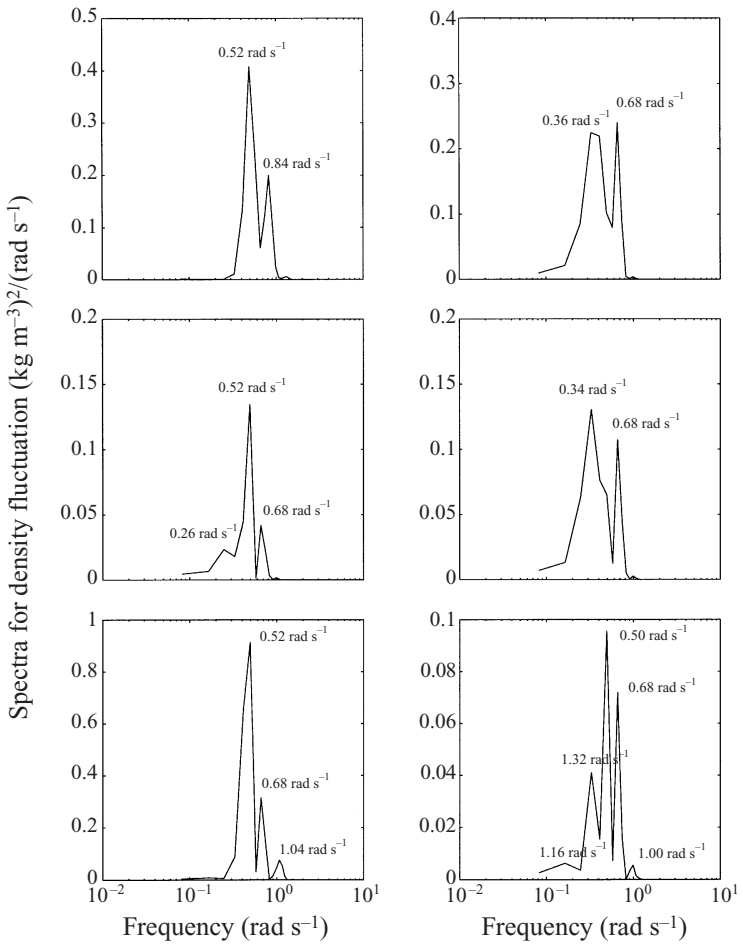


FIGURE 18. Spectra for density fluctuations at six locations within the interaction region, $Ri_m = 4.18$, $Ke = 0.225$, $Pr = 700$ and $Re = 32\,500$. Both superharmonic and subharmonic modes are excited.

They reported the excitation of the combination of difference frequencies within the interaction region for the bimodal type. The ratio between the half-width $\{(rv)/[2(N^2-\omega^2)^{1/2}]\}^{1/3}$ that the beam would have for viscous waves from a point source, at distance r from the source, and the half-width a that it would have for inviscid waves from an extended source of radius a in the form of

$$\frac{\{(rv)/[2(N^2-\omega^2)^{1/2}]\}^{1/3}}{a}$$

determines whether a given profile is unimodal or bimodal. The profiles are markedly unimodal when this ratio is larger than 0.4, and markedly bimodal when it is smaller than 0.2. The ratio for our case is about 0.01 confirming that the profiles are bimodal. Our early simulations and Teoh *et al.*'s (1997) experiments are also bimodal cases, with equal frequencies and wavelengths of two sources. Figure 12(*c*) of Teoh *et al.* (1997) and our results show the excitation of the divisions of the forcing frequencies as well as the multiples. However, as pointed out by Teoh *et al.* (1997), the maximum peak of the wave energy was at 2ω for the excited modes and wave energy at the divisions was negligible.

https://doi.org/10.1017/S0022112000008594 Published online by Cambridge University Press

4. Conclusion

A two-dimensional finite volume code has been validated for the prediction of internal wave dynamics in a stratified fluid. The code has been used to investigate the generation, propagation, reflection, and interaction of internal waves. The scheme can reproduce the behaviour of internal waves in a stratified fluid. The variation of wave slope with Reynolds number and wave angle with nonlinearity have been accurately predicted.

The model conserves energy. The interaction of the two symmetric internal wave beams quickly formed small spatial scales and a little later higher frequency motions. The energy was transferred to trapped higher modes by nonlinear interaction which, with time, caused overturning of the density field. This instability did not result from triad interaction, demonstrating that the triad interaction is not the only mechanism for transferring energy between waves of different frequencies. For non-symmetric wave–wave interaction both superharmonic and subharmonic modes were excited.

The analysis described above is a part of the first author's PhD study at the Department of Environmental Engineering, The University of Western Australia. Extensive computer resources were provided by the Centre for Environmental Fluid Dynamics (CEFD). The first author wishes to thank the Ministry of Jihade Sazandegi for providing a Scholarship and the CEFD for additional financial support.

REFERENCES

Appleby, J. C. & Crighton, D. G. 1987 Internal gravity waves generated by oscillations of a sphere. *J. Fluid Mech.* **183**, 439–450.

Armfield, S. W. 1991 Finite difference solutions of the Navier–Stokes equations on staggered and non-staggered grids. *Computers Fluids* **20**, 1–17.

Armfield, S. W. 1994 Ellipticity, accuracy and convergence of the discrete Navier–Stokes equations. *J. Comput. Phys. Fluids* **114**, 176–184.

Bretherton, F. P. 1964 Resonant gravity-wave interactions between waves. The case of discrete oscillations. *J. Fluid. Mech.* **20**, 457–479.

Chashechkin, Yu. D. & Neklyudov, V. I. 1990 Nonlinear interaction of bundles of short two-dimensional monochromatic internal waves in an exponentially stratified liquid. *Dokl. Earth Sci. Sect.* **311**, 235–238.

Davis, R. E. & Acrivos, A. 1967 Solitary internal waves in deep water. *J. Fluid Mech.* **29**, 593–607.

Dillon, T. M., Moum, J. N., Chereskin, T. K. & Caldwell, D. R. 1989 On the zonal momentum balance at the equator. *J. Phys. Oceanogr.* **19**, 561–570.

Fritts, D. C. 1989 Gravity wave saturation, turbulence and diffusion in the atmosphere: observation theory and implications. In *Parameterization of Small-Scale Processes, Proc. 'Aha Hulik'o' Hawaiian Winter Workshop*, pp. 219–234. University of Hawaii.

Gordon, D., Klement, U. R. & Stevenson, T. N. 1975 A viscous internal wave in a stratified fluid whose buoyancy frequency varies with altitude. *J. Fluid Mech.* **69**, 615–624.

Gregg, M. C. 1989 Scaling turbulent dissipation in the thermocline. *J. Geophys. Res.* **94**, 9686–9698.

Han, T. Y., Meng, J. C. S. & Innis, G. E. 1983 An open boundary condition for incompressible stratified flows. *J. Comput. Phys.* **49**, 276–297.

Harlow, F. H. & Welch, J. E. 1965 Numerical calculation of time–dependent viscous incompressible flow of fluid with free surface. *Phys. Fluids* **8**, 2182–2189.

Hasselmann, K. 1962 On the non-linear energy transfer in a gravity-wave spectrum. Part 1. General theory. *J. Fluid. Mech.* **12**, 481–496.

Hasselmann, K. 1966 Feynman diagrams and interaction rules of wave-wave scattering processes. *J. Fluid. Mech.* **30**, 737–739.

Hirt, C. W. & Cook, J. L. 1972 Calculating three-dimensional flows around structures and over rough terrain. *J. Comput. Phys.* **10**, 324–340.

https://doi.org/10.1017/S0022112000008594 Published online by Cambridge University Press

Hurley, D. G. 1969 The emission of internal waves by vibrating cylinders. *J. Fluid Mech.* **36**, 657–672.

Imberger, J. & Ivey, G. N. 1991 On the nature of turbulence in a stratified fluid. part 2: application to lakes. *J. Phys. Oceanogr.* **21**, 659–680.

Imberger, J. & Patterson, J. C. 1990 Physical limnology. *Adv. Appl. Mech.* **27**, 303–473.

Javam, A. 1995 Role of internal waves in subsurface mixing. PhD, University of Western Australia.

Javam, A., Teoh, S. G., Imberger, J. & Ivey, G. N. 1995 Two intersecting internal wave rays: A comparison between numerical and laboratory studies. In *Physical Processes in Lakes and Oceans. AGU, Coastal and Estuary Studies* vol. 54, pp. 377–388.

Kistovich, A. V. & Chashechkin, Yu. D. 1991 Nonlinear interaction of two-dimensional packets of monochromatic internal waves. *Izv. Atmos. Ocean. Phys.* **27**, 946–951.

Landau, L. D. & Lifshitz, E. M. 1987 *Fluid Mechanics*, 2nd edn. Pergamon.

Larsen, L. H. 1969 Oscillations of a neutrally buoyant sphere in a stratified fluid. *Deep-Sea Res.* **16**, 587–603.

Law, P., Peat, K. S. & Stevenson, T. N. 1982 An interferometer to study density stratified flows. *J. Phys.* E: *Sci. Instrum.* **15**, 1327–1331.

Leonard, B. P. 1979 A stable and accurate convective modeling procedure based on quadratic upstream interpolation. *Comput. Meth. Appl. Mech. Engng* **19**, 59–98.

Lin, C. L., Ferziger, J. H., Kossef, J. R. & Monismith, S. G. 1993 Simulation and stability of two-dimensional internal gravity waves in a stratified shear flow. *Dyn. Atmos. Oceans* **19**, 325–366.

Liu, R. 1989 A numerical and analytical study of internal waves in stratified fluids. PhD thesis, University of Manchester.

Liu, R., Nicolaou, D. & Stevenson, T. N. 1990 Waves from an oscillatory disturbance in a stratified shear flow. *J. Fluid Mech.* **219**, 609–619.

Lombard, P. N. & Riley, J. J. 1994 On the breakdown into turbulence of propagating internal waves. *4th Intl Symp. on Stratified Flows, Grenoble.*

McComas, C. H. & Bretherton, F. P. 1977 Resonant interaction of oceanic internal waves. *J. Geophys. Res.* **82**, 1397–1412.

McEwan, A. D. 1973 Interactions between internal gravity waves and their traumatic effect on a continuous stratification. *Boundary-layer Met.* **5**, 159–175.

McLaren, T. I., Pierce, A. D. & Murphy, B. L. 1973 An investigation of internal gravity waves generated by a buoyantly rising fluid in a stratified medium. *J. Fluid Mech.* **57**, 229–240.

Makarov, S. A., Neklyudov, V. I. & Chashechkin, Yu. D. 1990 Spatial structure of two-dimensional monochromatic internal-wave beams in an exponentially stratified liquid. *Izv. Atmos. Ocean. Phys.* **26**, 548–554.

Martin, S., Simmons, W. F. & Wunsch, C. I. 1972 The excitation of resonant triads by single internal waves. *J. Fluid. Mech.* **53**, 17–44.

Mowbray, D. E. & Rarity, B. S. H. 1967 A theoretical and experimental investigation of the phase configuration of internal waves of small amplitude in a density stratified fluids. *J. Fluid Mech.* **28**, 1–16.

Nicolaou, D. 1987 Internal waves around a moving body. PhD thesis, University of Manchester.

Nicolaou, D., Liu, R. & Stevenson, T. N. 1993 The evolution of thermocline waves from an oscillatory disturbance. *J. Fluid Mech.* **254**, 401–416.

Orlanski, I. 1976 A simple boundary condition for unbounded hyperbolic flows. *J. Comput. Phys.* **21**, 251–269.

Pao, Y. & Goldberg, A. 1969 *Clear Air Turbulence and Its Detection.* Plenum.

Patankar, S. 1980 *Numerical Heat Transfer and Fluid Flow.* Hemisphere.

Peat, K. S. 1978 Internal and inertial waves in a viscous rotating stratified fluid. *Appl. Sci. Res.* **33**, 481–499.

Peters, F. 1985 Schlieren interferometry applied to a gravity wave in a density-stratified liquid. *Exps. Fluids* **3**, 261–269.

Peyret, R. 1981 Numerical studies of nonhomogeneous flows. In *Advances in Fluid Mechanics* (ed. E. Krause). Lecture Notes in Physics, vol. 148, pp. 330–361. Springer.

Phillips, O. M. 1960 On the dynamics of unsteady gravity waves of finite amplitude. *J. Fluid Mech.* **9**, 193–217.

https://doi.org/10.1017/S0022112000008594 Published online by Cambridge University Press

PHILLIPS, O. M. 1966 *The Dynamics of the Upper Ocean*. Cambridge University Press.

SIMMONS, W. F. 1969 A variational method for weak resonant wave interactions. *Proc. R. Soc. Lond.* A **309**, 551–575.

STEVENSON, T. N. 1973 The phase configuration of internal waves around a body moving in a density stratified fluid. *J. Fluid Mech.* **60**, 759–767.

TEOH, S. G., IVEY, G. N. & IMBERGER, J. 1997 Experimental study of two intersecting internal waves. *J. Fluid Mech.* **336**, 91–122.

THOMAS, N. H. & STEVENSON, T. N. 1972 A similarity solution for viscous internal waves. *J. Fluid Mech.* **54**, 495–506.

THORPE, S. A. 1987*a* Transitional phenomena and the development of turbulence in stratified fluids: A review. *J. Geophys. Res.* **92**, 5231–5248.

THORPE, S. A. 1987*b* On the reflection of a train of finite-amplitude internal waves from uniform slope. *J. Fluid Mech.* **178**, 279–302.

https://doi.org/10.1017/S0022112000008594 Published online by Cambridge University Press